Eindhoven University of Technology
Department of Biomedical Engineering
Cardiovascular Biomechanics Research Group

Bachelor End Project

Creating vascular phantoms to verify biomechanical models of the carotid artery

Bram Volbeda
1007736

Supervisors:
dr. ir. R.G.P. Lopata
J. de Ruijter

Eindhoven, June 2019

Abstract

Cardiovascular diseases represent the leading cause of death worldwide, with ischemic stroke one of the most prevalent diseases. To prevent stroke patients undergo surgery, i.e. carotid endarterectomy. Only one in six patients benefits from this intervention however, so there is significant overtreatment of patients. To develop better treatment criteria to improve diagnosis and decision making, patient specific plaque composition and mechanical properties are needed. This study validated the elastography method to estimate the shear modulus using ultrasound in an inflation test setup and a neo-Hookean model. Vascular phantoms with different geometry and complexity were created for this experiment and the results were compared with what is considered the golden standard, a bi-axial tensile test. The results showed good agreement between the two methods, with $G_{US} = 42 \pm 5$ kPa and $G_{TT} = 37 \pm 6$ kPa. This study shows that the combination of ultrasound and biomechanical modelling has the potential of becoming an important clinical tool in vascular surgery.

Table of Contents

1. Introduction

1.1 General introduction

Currently, cardiovascular diseases (CVDs) represent the leading cause of death worldwide, being responsible for almost 50% of the total deaths in developed countries, and a rising number of deaths in low- and middle-income countries as a consequence of a rising occurrence of obesity and physical inactivity [Celermajer et al., 2012]. Of all the CVDs, stroke is one of the most prevalent diseases, and is an important cause for cardiovascular death or disability. It is defined as a sudden interruption of the blood supply of the brain, which can be caused by different mechanisms. By far the most common is an ischemic stroke, which occurs when an artery supplying the brain is blocked. This accounts for 88% of all strokes, and this can again be divided in two main types; thrombotic- and embolic ischemic stroke. Both occur when a cerebral artery supplying the brain becomes blocked by a blood clot. In the case of a thrombotic stroke this happens because the blood clot forms in the brain itself (this is the case in almost 50% of all strokes), while an embolic stroke is caused by a blood clot formed elsewhere in the body becoming obstructed in a cerebral artery [Nave et al., 2015].

An important risk factor in ischemic stroke is the narrowing of the artery as a consequence of plaque formation, i.e. atherosclerosis. Atherosclerosis is initially symptom-less, but one of the consequences can be plaque rupture, causing the high-occurring ischemic stroke. The current prevailing theory is that atherosclerosis is an inflammatory condition of the artery in response to injury. These responses are heaviest at branch points of arteries, such as the bifurcation of the carotid (see figure 1.1), as turbulent flow is prominent here, and therefore changes in shear stress occur at these sites [Elkind, 2006]. Shear stress in these areas is lower than arterial level hemodynamic shear stress, changing the phenotype of the artery's endothelial cells from an atheroprotective- to an atherogenic phenotype [Malek et al., 1999].

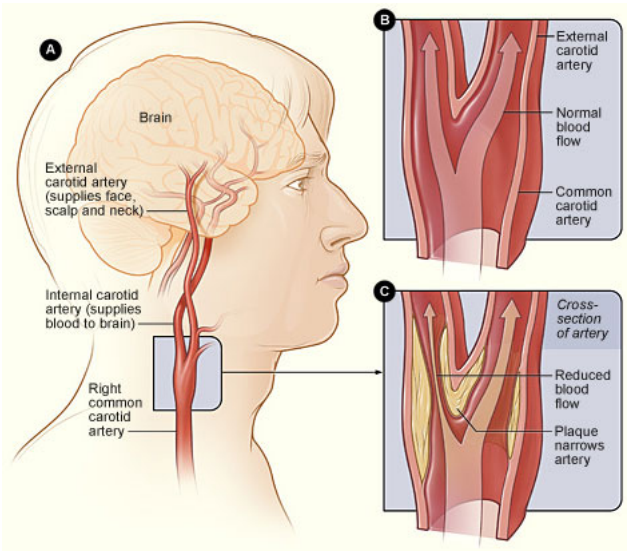

Figure 1.1: A) Bifurcation of the right common carotid artery into the internal- and external carotid artery. B) Blood flow around the bifurcation in a healthy carotid artery. C) Influence of plaque forming on blood flow. From surgery.ucsf.edu

The presence of a plaque in general is not enough to determine the stroke vulnerability of a patient; the morphology, composition and mechanical characteristics of the plaque play an important role in the risk of plaque rupture [Boekhoven, 2015]. Currently the degree of stenosis, i.e. the percentage of occlusion, is measured in the clinic by use of duplex ultrasound to determine if a patient should undergo carotid endarterectomy (CEA), in which the stenosis inside the artery is removed. Patients with a stenose greater than 70% undergo CEA, but for only one in six patients this

procedure is actually beneficial. Besides mortality risks of the operation (between 3-6%), a lot of patients are over-treated, and some patients with a stenosis lesser than 70% are not treated based on this geometrical criterion, while ischemic stroke also occurs in this population [Rothwell and Warlow, 1999].

One way the decision-making in the clinic could be improved is by taking into account plaque composition and its mechanical characteristics to better determine plaque vulnerability. Vulnerable, high-risk plaque is histologic different from stable, clinically asymptotic plaque. While non-invasive detection of plaque composition is difficult, ultrasonic characterization of the atherosclerotic plaque is currently possible and is regarded as one of the most promising fields of application in cardiovascular ultrasound imaging [Picano and Paterni, 2015]. Although a better predictor than stenosis severity alone, this imaging approach still has limitations, as not all plaques who rupture have the histologic features of vulnerability and vice versa; histologic vulnerable plaques do not always rupture [Picano and Paterni, 2015]. The plaque composition is linked to the plaque's mechanical properties, as changing necrotic core size, fibrous cap thickness and calcification has been shown to significantly alter mechanical properties [Teng et al., 2014]. Therefore a lot of research has been done already to obtain the mechanical properties of the carotid artery using strain imaging techniques. Ultrasound imaging (US) is the preferred method for this research, as it is able to obtain the geometry and deformation of the carotid artery, has a short scanning time, no radiation exposure (in contrast to computed tomography (CT)), and has a low cost. US is not able to distinguish the different components of the plaque, while magnetic resonance imaging (MRI) is. MRI however requires long scanning times, is expensive, and has a poor reproducability. While US still has quite some inter-observer variability, it is still the most frequently used imaging modality in the clinic [Vancraeynest et al., 2011].

A popular method to estimate 2-D strain is schematically depicted in figure 1.2 and is called vascular elastography. With this method the 2-D strains are estimated in the direction of the US beam, and combined with intraluminal pressure data the material properties of the vascular wall can be estimated [Lopata et al., 2014]. To do this a biomechanical model using a finite element method is used, wherein the Young's modulus distribution is optimized using this finite element method [Baldewsing et al., 2006] [Doyley et al., 2000].

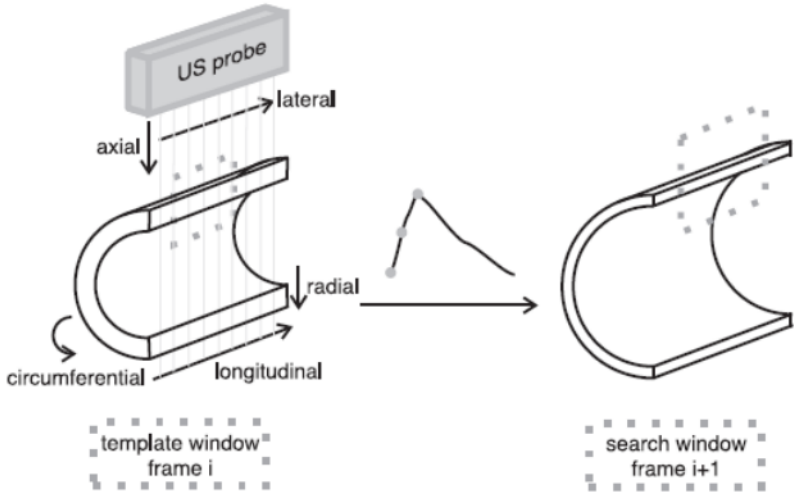

Figure 1.2: An illustration of a vessel before inflation (left) and at maximum inflation (right). The dotted rectangle represents the search window used for the displacement estimation [Boekhoven, 2015]

A phantom is a model of the body or a part of the body. Advantages of phantoms are that they are readily available and provide more consistent results than the use of a living subject or cadaver and therefore also avoids exposing subjects to risks. Vascular phantoms are models of human arteries and are used to evaluate imaging techniques such as US, angiography, and CT. Furthermore, validation of techniques like vascular elastography is typically performed on these phantoms. Vascular phantoms must meet specific requirements on the mimicking materials, as they are expected to mimic the mechanical properties of real vascular tissue [Dabrowski et al., 1997].

1.2 Aim of this project

This project focuses on the validation of the vascular elastography method. First, cylindrical polyvinyl alcohol cryogel (PVA-c) phantoms will be created with different geometry and complexity. These phantoms will be submitted to an inflation experiment to perform vascular elastography upon, and the resulting strain data will be used as with the pressure data as input for a neo-Hookean model to estimate the mechanical properties of the phantoms. Small samples of PVA-c were created to submit to a bi-axial tensile test, in which both the circumferential and longitudinal stretching were applied that closely matched the inflation experiment, and these results will be compared with the inflation test data. The results should show to which degree the elastography method is capable to accurately estimate the mechanical properties of the different phantoms.

2. Materials & Methods

2.1 PVA Phantoms

Polyvinyl alcohol cryogel (PVA-c) phantoms were created to mimick the carotid artery. An advantage of using phantoms is that the geometry and the stiffness of the phantom can be controlled. The latter by varying the number and duration of freeze/thaw cycles (f/t cycles) it is subjected to and the PVA concentration.

2.1.1 PVA preparation

For the preparation Mowiol (Mowiol 28-99, Sigma-Aldrich) with Mw 145,000, 99.0-99.8 mol% hydrolysis was used. A solution of 15 wt% PVA in demineralized water was prepared. Because of the setup used in this lab, the maximum amount of PVA that could be synthesized in one batch was about 100 mL. The reason for this is that the stir bean is not able to appropriately stir the solution to obtain a homogeneous solution if this amount is exceeded. Depending on the setup however, this amount could be increased. The solution was heated to approximately 85 °C and stirred with a magnetic stir bean for about 2 hours, until the solution was homogeneous. Hereafter an ultrasound scatterer was added (Orgasol 2001, Arkema France) in 1.2 wt%, with an average size of 5.8 m, and the solution was manually stirred. The PVA solution is now ready to be used for the phantoms. A complete protocol can be found in the Appendix.

2.1.2 Phantom preparation

The molds used are axi-symmetric cylindrical Perspex molds for the outside, and a stainless steel bar for the inside (lumen). This created a single layer phantom with an inner diameter D_{lumen} of 5 mm and an outer diameter D_{outer} of 8 mm. For the phantoms with a stenosis there was chosen for 60% stenosis. This gives $D_{stenosis}$ equal to 2 mm, which gradually increases to D_{lumen}, see figure 2.1. The phantoms were subjected to four f/t cycles to increase their stiffness, with one cycle consisting of 16 hours of freezing at - 20 °C and 8 hours of thawing at room temperature. When the phantoms are finished, they can be preserved for years at 5 °C in purified water [Ruijter, 2016].

(a) **(b)**

Figure 2.1: **(a)** Dimensions of the phantoms. The phantoms have an outer diameter of 8 mm and an inner diameter of 5 mm. There is one exception, namely the tubed phantoms, who have an inner diameter of 3 mm. **(b)** Example of a standard phantom with stenosis 60% stenosis.

The phantoms are a simplified model of an artery, consisting of a single layer, while an artery consists of three layers that can be combined into an inner layer (intima) and an outer layer (adventitia). Of these two layers, the adventitia is the stiffer layer and thought to be dominant in the limitation of acute overdistension in vessels [Humphrey, 2002]. For these reasons the single layer will try to mimick the outer layer as this is the most important layer in determining the vessel's mechanical behaviour.

2.1.3 Phantom creation

Different kinds of phantoms were created in this project trying to mimick the calcification of an artery. To rate the degree of success (i.e. their capability to (locally) stiffen the phantom) of these attempts they had to be compared to phantoms without a calcification and/or stenosis. Different methods were used to try to create a calcification. First, a phantom without stenosis (referred to as a 'normal' phantom from now on) was attempted to stiffen by mixing the PVA solution with silicon carbide (SiC) particles (SiC, Sigma-Aldrich) to a total of about 20 wt%. The density of the SiC particles is 3.16 g/cm^3, while that of PVA is about 1.2 g/cm^3. The size of the particles is -400 mesh of $\geq$ 97.5%, which means that at least 97.5% of the particles is smaller than 37 m, the order of magnitude for beginning calcifications in arteries [Curtze et al., 2016]. Secondly, a phantom with stenosis was created and $CaCO_3$ particles of about 2 mm^3 were tried to put around the stenosis to locally stiffen the area around the stenosis. $CaCO_3$ has a density of 3.14 g/cm^3 and is an important compound in the composition of calcifications in vivo [Curtze et al., 2016].

For the third method a different mold was used. The Perspex mold is still used for the outside, but the lumen is a stainless steel bar with a diameter D_{lumen} of 3 mm. This gives a wall thickness of 2.5 mm. The plug to seal one end of the Perspex tube had three small holes, dividing the plug in three equal parts of each 120° in which steel bars with $D_{bar,mold}$ of 1 mm could be plugged. After the four f/t cycles this would create small hollow tubes which could be filled with other mixtures or materials to try to increase the stiffness. The phantoms created with this method were normal phantoms. One phantom had two of those tubes, which were filled with a mixture of PVA and SiC in about 50 wt%. The SiC had to be mixed with PVA because the particles are so refined they would be sprayed all around when contacted with a small stream of air. Two tubes were used because this would better illustrate the local effects of adding a stiffer mixture instead of global effects on stiffness. Another phantom had three tubes of which two were filled with the same mixture as described above, and one with a stainless steel bar with D_{bar} of 0.9 mm. This third tube was added to discover the impact of the addition of a very stiff compound to local stiffness and global stiffness compared to the two tube phantom. The mold described in this paragraph is only used for these two phantoms.

The last method to mimick calcification employed PLA, which is a material used in 3D printing. The same mold as in the first two methods was used. A diameter D_{PLA} of 1 mm, a high stiffness, and an adjustable length make this a material that can be placed more precisely around the stenosis. The result is two phantoms with two pieces of about 15 mm long positioned around the stenosis.

Besides the creation of phantoms with calcifications other phantoms were created; a normal phantom (i.e. without stenosis or calcification), a phantom with only the stenosis, and phantoms with a gradient in stiffness. The latter were created by adding for three subsequent days one small layer of PVA and thereafter one additional f/t cycle. This resulted in a phantom consisting of different areas, each submitted to 4/3/2 f/t cycles respectively. When creating this type of phantom, the width of the imaging probe used is especially important, as the transitions should be visible within this dimension. The results of these phantoms during the inflation test should be interesting to observe as it could tell something about the influence of adjacent tissue on local strain behaviour.

2.2 Bi-axial tensile test

2.2.1 Sample preparation

To get an estimation of the stiffness of the phantoms, PVA samples submitted to the same number of freeze/thaw cycles were created. In order to do this a square mold was used to get PVA with a size of about 80x90 mm. For three consecutive days the mold would be opened after the f/t cycle and about one third of the initial sample size was cut off and preserved in the fridge in purified water. This results in samples with two, three and four f/t cycles, also present in the phantoms. All phantoms had four f/t cycles, except the gradient phantoms who have 2/3/4 f/t cycles. The larger samples were cut into smaller samples of 20x20 mm and 10x10 mm, and these samples were used for the bi-axial tensile test. This procedure was done multiple times. The thickness was varied to agree with the dimension of the wall thickness in the phantom molds, i.e. 1.5 mm. Of the 2.5 mm samples only the 4 f/t cycles was made, to verify the script used for G value estimation.

2.2.2 Equations bi-axial tensile test

After sample preparation, the samples were be mounted in the bi-axial tensile tester (CellScale, Waterloo,ON, Canada), using a 2.5 N loadcell.

First, the rakes (five tines with a spacing of 2.0 mm for a total width of 10 mm) are attached in the z-direction (corresponding the longitudinal direction) with a distance between the rakes of 10 mm for the 20 x 20 mm samples and about 7 mm for the 10 x 10 mm samples. The sample would then be prestretched with a stretch λ_{zz} of 1.2, with stretch being defined as:

$$\lambda = \frac{L}{L_0} \tag{2.1}$$

with L_0 the original length of the sample and L the current length.

If we assume incompressibility, i.e. $\lambda_{xx} \cdot \lambda_{yy} \cdot \lambda_{zz} = 1$, the deformation tensor $\mathbf{F}_0$ is given by

$$\mathbf{F}_0 = \begin{vmatrix} \frac{1}{\sqrt{\lambda_{zz}}} & 0 & 0 \\ 0 & \frac{1}{\sqrt{\lambda_{zz}}} & 0 \\ 0 & 0 & \lambda_{zz} \end{vmatrix} \tag{2.2}$$

After prestretching, the rakes in the y-direction (corresponding to the circumferential direction) are mounted, again 10 mm or 7 mm apart, depending on the sample. While the stretch in the z-direction is held constant, the sample is stretched in the y-direction to a stretch λ_{yy} equal to 1.5 over the duration of 25 s, giving a strain rate of 0.02 s^-1. This gives the following equation for $\mathbf{F}_1$

$$\mathbf{F}_1 = \begin{vmatrix} \frac{1}{\lambda_{yy}} & 0 & 0 \\ 0 & \lambda_{yy} & 0 \\ 0 & 0 & 1 \end{vmatrix} \tag{2.3}$$

The total deformation tensor is then given by eq. 2.4:

$$\mathbf{F} = \mathbf{F}_0 \cdot \mathbf{F}_1 = \begin{vmatrix} \frac{1}{\sqrt{\lambda_{zz}} \cdot \lambda_{yy}} & 0 & 0 \\ 0 & \frac{\lambda_{yy}}{\sqrt{\lambda_{zz}}} & 0 \\ 0 & 0 & \lambda_{zz} \end{vmatrix} \tag{2.4}$$

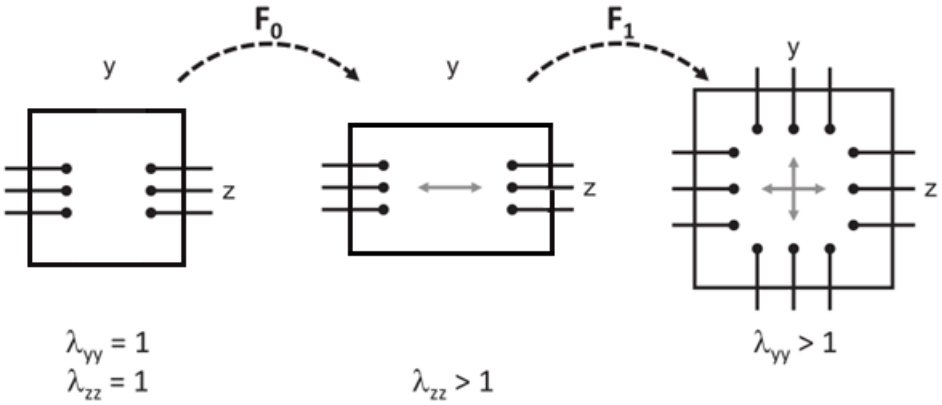

Figure 2.2: schematic overview of the method used to prestetch the sample (λ_{zz}) and attach the rakes to apply stretch in the y-direction (λ_{yy}). Adapted from [Lopata et al., 2014].

After the sample reaches a stretch λ_{yy} of 1.5 the sample is immediately relaxed to the initial state after prestretch over the duration of 25 s. This is done for a total of three cycles. The multiple steps are depicted in figure 2.2.

The mechanical behaviour is modelled as a neo-Hookean solid. This model is valid for large deformations and assumes a linear elastic, isotropic behaviour and incompressibility of the tissue. For neo-Hookean solids the stress-stretch relationship is given by

$$\sigma = -p_0 I + G(B - I) \tag{2.5}$$

σ is the Cauchy stress tensor, p_0 an undetermined hydrostatic stress, I the identity matrix, G the shear modulus and B the left Cauchy-Green deformation tensor.

The definition of the left Cauchy-Green deformation tensor B is

$$B = F \cdot F^T \tag{2.6}$$

which gives with eq. 2.3:

$$B = \begin{vmatrix} \frac{1}{\lambda_{zz} \cdot \lambda_{yy}^2} & 0 & 0 \\ 0 & \frac{\lambda_{yy}^2}{\lambda_{zz}} & 0 \\ 0 & 0 & \lambda_{zz}^2 \end{vmatrix} \tag{2.7}$$

If plane stress is assumed, i.e. $\sigma_{xx} = 0$, an expression for p_0 can be obtained

$$\sigma_{xx} = -p_0 I + G(\frac{1}{\lambda_{zz} \cdot \lambda_{yy}^2} - 1) = 0 \tag{2.8}$$

$$p_0 = G(\frac{1}{\lambda_{zz} \cdot \lambda_{yy}^2} - 1) \tag{2.9}$$

Now eq. 2.8 substitued in 2.4 gives for σ_{yy}

$$\sigma_{yy} = -G(\frac{1}{\lambda_{zz} \cdot \lambda_{yy}^2} - 1) + G(\frac{\lambda_{yy}^2}{\lambda_{zz}} - 1) \tag{2.10}$$

$$\sigma_{yy} = \frac{G}{\lambda_{zz}}(\lambda_{yy}^2 - \frac{1}{\lambda_{yy}^2}) \tag{2.11}$$

2.2.3 Estimation of the shear modulus

With the help of the neo-Hookean model the shear modulus G can be estimated after submitting a sample to the tensile test. The stretch λ_{yy} can simply be calculated with eq.2.1 (NB: L_0 is the length after prestretching!), and the Cauchy stress σ_{yy} can be calculated with the force of the rakes and the area this force acts on, by

$$\sigma_{yy} = \frac{F_{rakes}}{A} \tag{2.12}$$

Now for every point in time all variables of eq. 2.11 are known, except shear modulus G. A script was written in MATLAB (The Mathworks, Natick, MA, USA) to estimate G. If G is left out of the right hand side of eq. 2.11 and what is left is called RHS, i.e.

$$RHS = \frac{1}{\lambda_{zz}}(\lambda_{yy}^2 - \frac{1}{\lambda_{yy}^2}) \tag{2.13}$$

a plot can be made between σ_{yy} and RHS, of which the slope will be equal to G. Hence an estimation for G can be obtained.

2.3 Inflation test

2.3.1 Set-up

To simulate the deformation of a pulsating carotid, an experimental set-up developed by Van den Broek et al. [van den Broek et al., 2011] is used. It consists of a pump which is controlled with software called LabView (National Instruments, Texas, USA), an organ bath and a set of tubes connecting the pump and the organ bath to each other. The pulsation frequency and the pulsation strength can be controlled. For this experiment the frequency was set on 1 Hz (60 bpm) and the pressure ranged from about 0 mmHg to 45 mmHg, which is a normal pulse pressure for a person in rest [Klabunde, 2011]. The phantom is mounted between two stainless steel bars in the organ bath and prestretched to a λ_{zz} of about 1.2. Between the pump and the steel bar a pressure sensor is connected. On the other side of the phantom a syringe is attached to a three-way stopcock to function as a Windkessel, and the tubes connected to this stopcock lead to a water bath. Another tube connected to the pump draws its water supply from this water bath. This is to prevent the flow of air bubbles in the system. See figure 2.3 for a schematic overview of the set-up.

2.3.2 Data acquisition

Ultrasound imaging was performed with a MyLab70 ultrasound system (Esaote Europe, Maastricht, Netherlands) equipped with a 2-D linear array transducer (LA435) with a lateral sampling of 50 RF lines/cm and recording 44 frames/s in 2D B-mode. Eight pulsation cycles are imaged, giving eight seconds of image data and a total of 352 frames. The data was digitized with a sampling rate of 50 MHz and transmitted to a workstation called ArtLAB (ArtLAB, Esaote). The ultrasound probe is placed above the phantom in longitudinal direction, just below the water surface, and at the center of the phantom to avoid boundary conditions caused by cannulation. The RF data and the pressure data were used for further analysis.

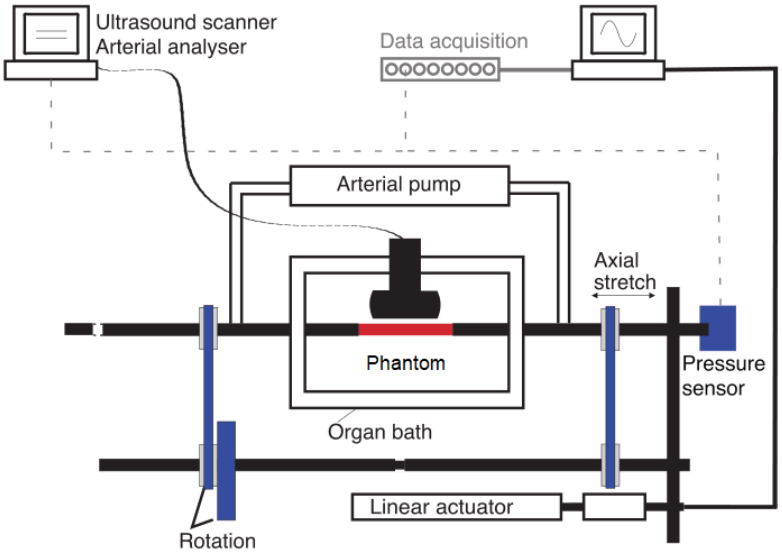

Figure 2.3: Schematic setup for the inflation test. Adapted from [Boekhoven, 2015]

2.3.3 Data processing

The data was imported in MATLAB and will be processed using a 2-D coarse-to-fine displacement estimation algorithm, meaning that the displacement will be roughly estimated using only the signal envelope, and this estimate will be used to align the search area in the current iteration, enabling the use of smaller segments of RF data [Lopata et al., 2009] [Chen et al., 2007]. This will be done for two iterations. First however, segmentation of the data is necessary to obtain a geometry for further analysis and a region of interest (ROI). The desired frames of one pulsation are selected from M-mode view, from the minimum to the maximum diameter of the phantom, see figure 2.4. Subsequently the upper outer wall and -luminal wall and lower outer wall and -luminal wall are segmented manually in a B-mode image. Between the segmentation lines a grid of tracking points is constructed, and the displacements are estimated with the algorithm described above. The displacement field were then filtered using a median filter to remove outliers, and from this displacement field the strains are calculated, see figure 2.5. Because of the positioning of the ultrasound probe, the phantom is imaged in the longitudinal and radial direction, and only these strains can be calculated. The longitudinal strain is set to zero because this improves the stability of the mesh during displacement tracking, and longitudinal strains are found to be significantly lower than radial strains [Larsson et al., 2015]. Furthermore, the lateral displacement is dependent on the temporal resolution of the US device. The output of the algorithm is the radial strain for each frame selected earlier.

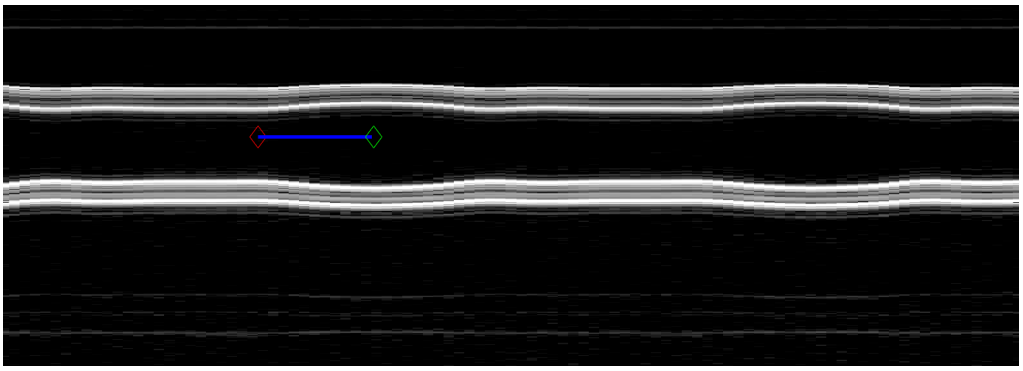

Figure 2.4: M-mode view of a normal phantom. The red diamond indicates the starting frame (diameter is minimal) while the green diamond indicates the end frame (diameter is maximal)

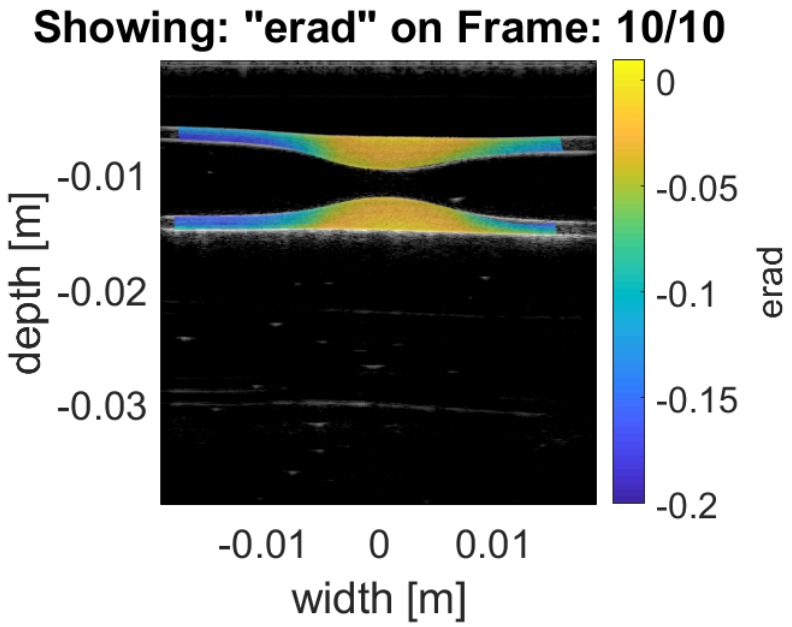

Figure 2.5: The radial strains estimated by the script after manually indicating the border of the upper- and lower wall. The mesh used for this example consists of 6x70 points.

2.3.4 Equations and estimation of the shear modulus

Like the bi-axial tensile test, equations can be derived for the inflation test to estimate the shear modulus G. Because the protocol for the inflation test is analogous with that of the tensile test, i.e. first applying a prestretch and then forcing a strain in one direction while maintaining the prestretch in the other, and the mechanical behaviour is still modelled as a neo-Hookean solid, the equations described in section **2.2.2** also hold for the inflation test. Instead of Cartesian coordinates (x,y,z), a cylindrical coordinate system (r, ϕ, z) is used however. This means that eq. (2.11) transforms into the following equation:

$$\sigma_{\theta\theta} = \frac{G}{\lambda_{zz}}(\lambda_{\theta\theta}^2 - \frac{1}{\lambda_{\theta\theta}^2}) \tag{2.14}$$

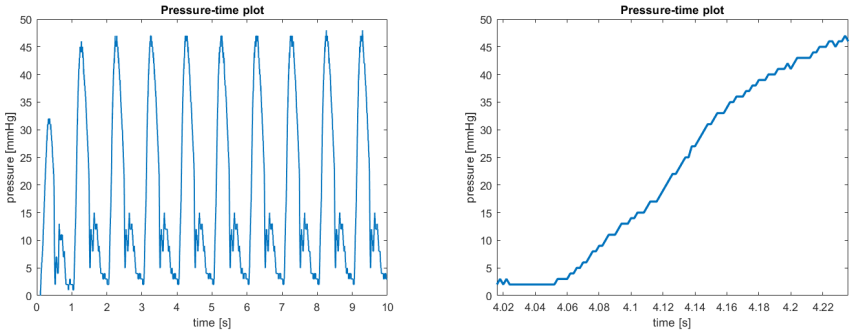

Figure 2.6: **(a)** The total pressure curve for a phantom during the inflation test. A transient response can be observed during the first three pulses/seconds. **(b)** Cut-out fragment of the pressure data which represents the pressure responsible for the change from minimal diameter to maximal diameter. The script will sample this curve with a number of equidistant points equal to the number of frames selected. Each pressure data point then corresponds to a specific frame.

with $\lambda_{\theta\theta}$ the circumferential stress, defined by:

$$\lambda_{\theta\theta} = \frac{d_p}{d_0} \tag{2.15}$$

and d_p the pressure dependent diameter and d_0 the diameter of prestretch. Because the walls of the phantom are relatively thick-walled, the diameter is defined as the middle of the outer and inner wall, and calculated with:

$$d = \frac{d_{outer} + d_{inner}}{2} \tag{2.16}$$

This is done for every tracking position in longitudinal direction and for every frame.

Of course the calculation of $\sigma_{\theta\theta}$ is different than that of σ_{yy}. For the inflation test, the circumferential stress is estimated using Laplace's law:

$$\sigma_{\theta\theta,LP} = \frac{p \cdot d_p}{2h_p} \tag{2.17}$$

with h_p the pressure dependent wall thickness. The wall thickness is calculated for every tracking position in longitudinal direction and for every frame by taking the difference between the y-value of the outer wall and the inner wall.

Analogous to the tensile test all variables are known except the value of G. G is omitted again of the right hand side of eq. (2.4), and the remainder is called RHS:

$$RHS = \frac{1}{\lambda_{zz}}(\lambda_{\theta\theta} - \frac{1}{\lambda_{\theta\theta}}) \tag{2.18}$$

The slope of the plot between $\sigma_{\theta\theta}$ and RHS will now equal to G.

To determine the pressure on each frame, a segment of the total pressure data is cut out, representing the pressure curve from minimal diameter to maximal diameter. The pressure data of the first three pulses (corresponding to three seconds) is ignored as a transient response is observed in these first pulses. An example of a pressure signal and the corresponding 'filtered' pressure can be seen in figure 2.6.

3. Results

3.1 Tensile test

The results of the tensile test are presented in figure 3.1. With the script described in the Materials & Methods section the shear modulus of each sample was estimated. A total of thirteen samples was created; 1 sample of 1 f/t cycle, 3 samples of 2 f/t cycles, 3 samples of 3 f/t cycles, 4 samples of 4 f/t cycles, 1 sample of 5 f/t cycles and 1 sample of 4 f/t cycles but a thickness of 2.5 mm. Some samples were subjected to multiple tests, so the number of data points in figure 3.1 is higher than the number of samples. The typical stress-strain curve and its associated values for a sample with 4 f/t cycles is also seen in the figure below.

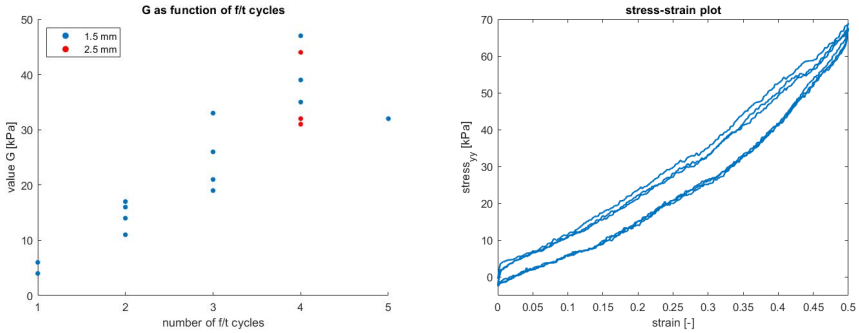

(a) **(b)**

Figure 3.1: **(a)** Scatterplot of the value of G as a function of the number of f/t cycles. The blue dots represent samples with a thickness of 1.5 mm, the red dots samples with a thickness of 2.5 mm. Thickness should not be a factor that changes the outcome for G, because an increase in area also results in an increase in force and therefore stress remains fairly constant. By varying the thickness however, the script that calculates the value of G can in part be validated, as results for 2.5 mm and 1.5 mm samples should not deviate much. **(b)** Stress-strain curve of 4 f/t sample. It demonstrates that the PVA material does not show linear elastic behaviour.

3.2 Inflation test

3.2.1 General results

For each sample the shear modulus G was estimated using the MATLAB script described in section **2.3.4**. The results are shown in table 3.1. Figure 3.2 **(a)** shows an example of the dissection of a phantom with stenosis into three sections. Of each of these three sections the shear modulus is estimated as well, along with the local change in diameter, wall thickness and radial strain. Figure 3.2 **(b)** shows the radial strains for a specific frame. Strains in the area around the stenosis are lower compared to strains outside the stenosis area. The relative diameters of each section and the phantom in total as response to the applied pressure are shown in Figure 3.2 **(c)**. For the pressure interval only the pressure values are chosen that correspond to the B-mode frames from minimal to maximal diameter. Last, both the upper- and lower wall were divided into three segments: an outer wall, a middle wall and an inner wall. Of each of these segments the strain is calculated in response to the applied pressure, see figure 3.2 **(d)**.

Inflation Test Data				
Phantom	G total	G section I	G section II	G section III
No calcification				
Normal	45	49	43	43
Stenosis (1)	46	45	58	50
Stenosis (2)	36	43	42	46
Calcification				
SiC	58	53	64	55
$CaCO_3$	45	48	53	51
Two tubes	85	86	88	78
Three tubes	65	79	52	54
PLA	65	70	80	85
Gradient phantoms				
Gradient (1)	29	19	35	50
Gradient (2)	31	22	32	57

Table 3.1: Shear modulus G for the total phantom and the three separate sections of each phantom. The values for G are in kPa. Section I corresponds to the left of the image, section II to the middle, and section III to the right side of the B-mode image.

3.2.2 Phantoms without calcifications

An example of the results of one data set is already depicted in figure 3.2, that of stenosis (1). Stenosis (2) showed similar strain behaviour in response to pressure as stenosis (1). The normal phantom has an even distribution of G. In contrast to the stenosis samples, the strains are not necessarily higher in the lower wall compared to the upper wall. The strains on the outer segments of both the upper- and lower wall on the other hand are lower than the strains of the middle- and inner segments. This results is also found in the phantoms with stenosis. The phantoms without calcifications can be used as reference for the phantoms with calcifications.

3.2.3 Phantoms with calcifications

The first attempt to calcification was the addition of SiC particles. This phantom has no stenosis, so the results will be compared to the normal phantom. In comparison to the normal phantom the difference in shear modulus is relatively small. (58 kPa vs 45 kPa). For both the $\sigma_{\theta\theta}$ - RHS relationship is depicted in figure 3.3.

The phantom with $CaCO_3$ shows no significant difference in shear modulus compared to the stenosis phantoms without calcification (45 kPa vs $\approx$ 40 kPa). The strain behaviour is also identical, both in relative terms as absolute terms, with a higher strain around the stenosis area and lower strains outside these areas. Only the change in relative diameter of section I seems to somewhat differ between the two phantoms. The relative diameters of each section are depicted in figure 3.4.

The calcified phantoms with two- and three tubes show a higher value for the shear modulus (85 kPa and 65 kPa for the two - and three tube phantom respectively) in comparison to the normal phantom (45 kPa). The strains in the tubed phantoms are also significantly lower compared to the normal phantom. The strain in the two tube area is also lower in the area of the 'calcification' compared to the other areas, see figure 3.6. This does not show in a different value for G for the different sections, however. This effect is not observed in the three tube phantom. Both phantoms show a higher strain at the upper- and lower inner wall, as is also observed with the normal phantom.

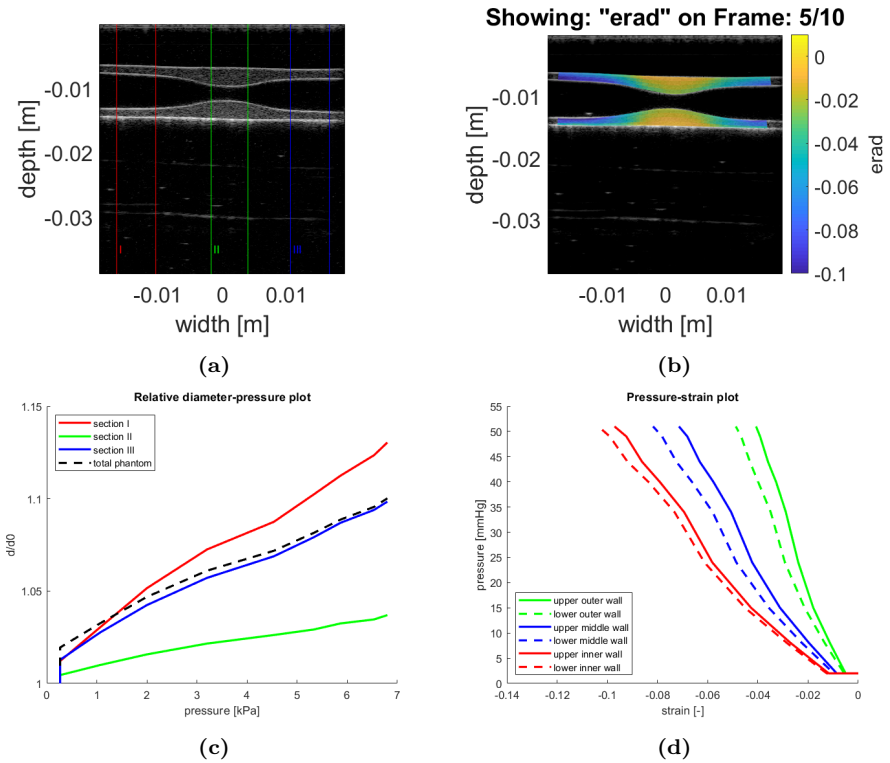

Figure 3.2: **(a)** B-mode image of phantom - stenosis (1). The figure shows the three sections the phantom is divided into; section I (red), section II (green) and section III (blue). Local diameter, wall thickness, strain and shear modulus are estimated for each section. **(b)** The radial strain of the upper- and lower wall. The data shows that radial strain is not evenly distributed; the strain around the stenosis is lower than outside the stenosis. Strains are negative because compression is per definition a negative strain. **(c)** The relative diameter of each section in relation to the applied pressure. Note that for the pressure the interval is chosen that corresponds to the frames earlier selected for strain estimation, i.e. from minimal diameter to maximal diameter. **(d)** Pressure-radial strain relations for each segment of the upper- and lower wall. Note that these segments are not the sections seen in **(a)** and **(c)**, but each wall divided into three layers horizontally; the outer wall, middle wall and inner wall. The data shows that each segment of the lower wall has a higher strain at a fixed pressure compared to their upper wall counterpart.

The last calcification was a stenose phantom with PLA. The value for the shear modulus is higher compared to the stenosis phantom without calcification (65 kPa vs $\approx$ 40 kPa). This is also reflected in the change of relative diameter between the phantoms when applying pressure. The maximal change in relative diameter is about a factor three lower for the PLA phantom than for uncalcified stenosis phantom, see figure 3.5.

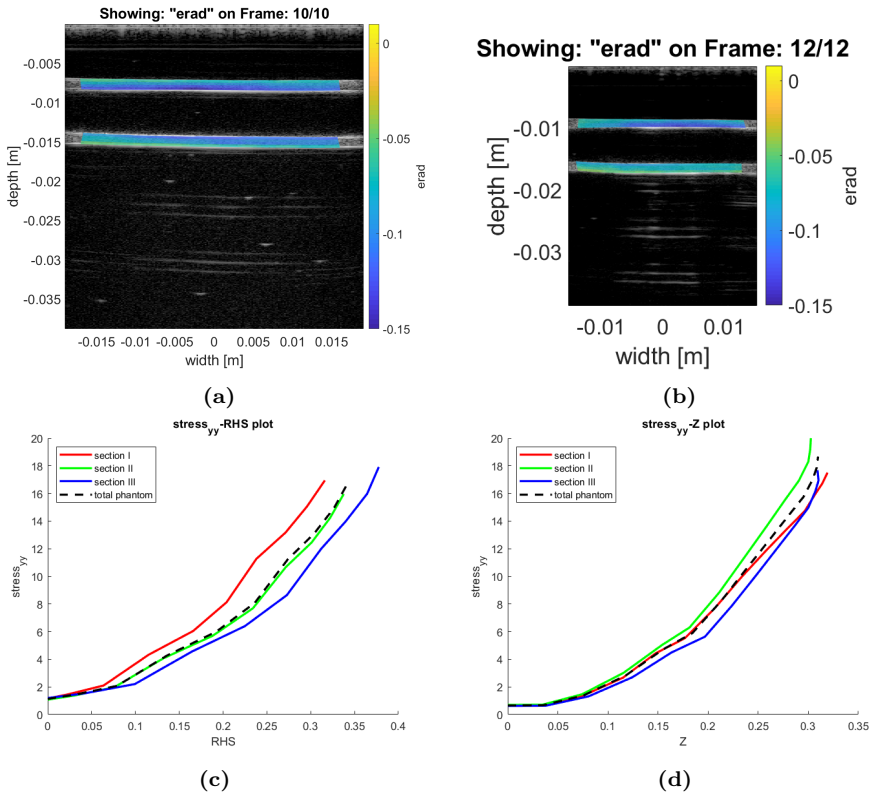

Figure 3.3: Radial strain at maximal distention of the normal phantom **(a)** and the SiC phantom **(b)**. $\sigma_{\theta\theta}$ verus RHS for the normal phantom **(c)** and the SiC phantom **(d)**. For the SiC phantom the slope is almost equal to that of the normal phantom, resulting in an fairly equal shear modulus. Note that the axis names are off; σ_{yy} corresponds to $\sigma_{\theta\theta}$ and Z corresponds to RHS.

3.2.4 Phantoms with gradient

The phantoms were imaged with the least stiff section on the left, and the most stiff section on the right, i.e. 2-3-4 f/t cycles. This is reflected in the estimation of the shear modulus, as for both gradient phantoms the shear modulus increases with each section, corresponding to an increase of the number of f/t cycles, see figure 3.7. The shear modulus of the total gradient phantoms deviates from the value for the normal phantom ($\approx$ 30 kPa vs 45 kPa), but the shear modulus of the section that corresponds to 4 f/t cycles (section III) is similar to the total shear modulus of the normal phantom ($\approx$ 50 kPa vs 45 kPa), which is also submitted to 4 f/t cycles. In figure 3.7 the division of both gradient phantoms into three sections can be seen, as well as the radial strain at maximal distention and the pressure - relative diameter relationship for both gradient phantoms.

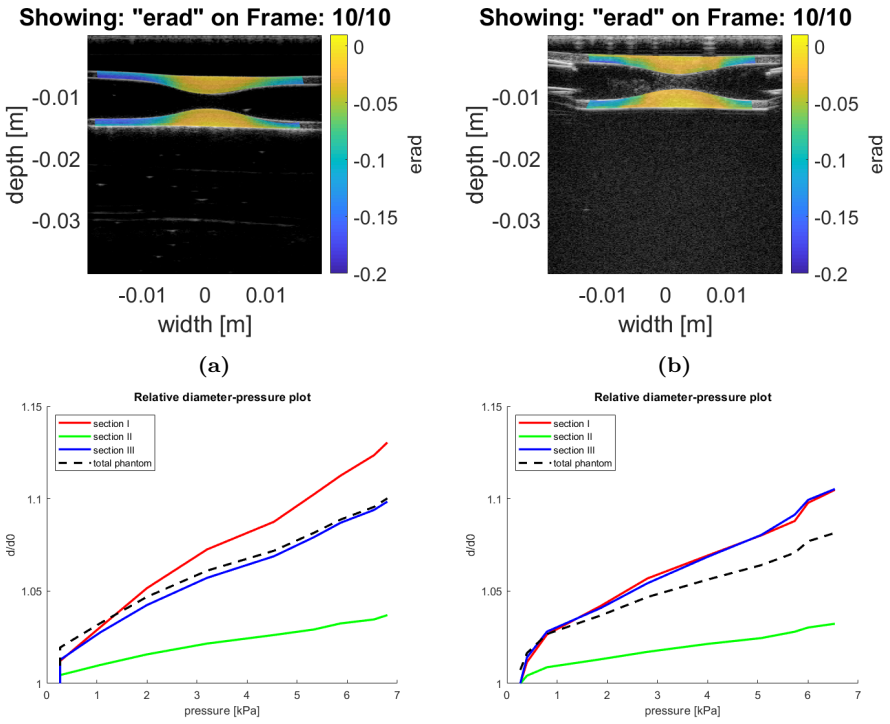

Figure 3.4: Radial strain images at maximal distention of the uncalcified stenosis phantom **(a)** and the $CaCO_3$ phantom **(b)**. The area where the phantos are cannulated can be seen on the edges of **(b)**. Relative diameter d/d_0 versus the applied pressure (in kPa) for the stenosis phantom without calcification **(c)** and the phantom with a $CaCO_3$ calcification **(d)**.

3.2.5 Tensile test versus inflation test

Except for the gradient phantoms, all phantoms were subjected to 4 f/t cycles. The estimation of the shear modulus from the tensile test can be compared to the results of the inflation test. Neglecting the phantoms with calcification, the value for G_{US} is 42 ± 5 kPa. The value from the tensile test G_{TT} has a value of 37 ± 6 kPa. The gradient phantoms can be compared to the tensile test samples corresponding to two, three and four f/t cycles. The value for the 2 f/t cycles is 21 ± 2 kPa for $G_{US,2}$ and 15 ± 3 kPa for $G_{TT,2}$. For 3 f/t cycles the value of $G_{US,3}$ was found to be 34 ± 2 kPa and $G_{TT,3}$ was equal to 25 ± 6 kPa. The 4 f/t cycles samples had a $G_{US,4}$ of 42 ± 5 kPa and a $G_{TT,4}$ of 37 ± 6 kPa. The shear modulus estimated by the tensile test is for each different category lower than their inflation test counterpart. In both models, an increasing number of f/t cycles leads to an increase of the shear modulus, as is expected.

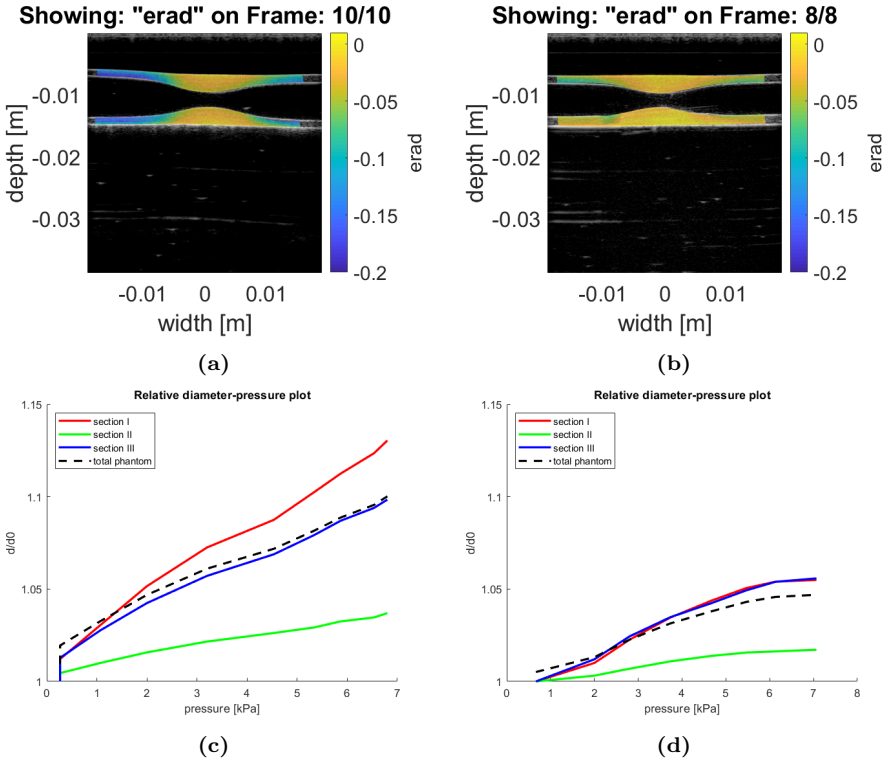

Figure 3.5: The radial strain at maximal distention for the uncalcified stenosis phantom **(a)** and the PLA phantom **(b)**. Strains are overall lower in the PLA phantom, even outside the stenosis area. The relative diameters as response to applied pressure are found in **(c)** for the uncalcified stenose phantom and in **(d)** for the PLA phantom. Changes in diameter are substantially lower in the PLA phantom, even showing a decrease by a factor of three for section I.

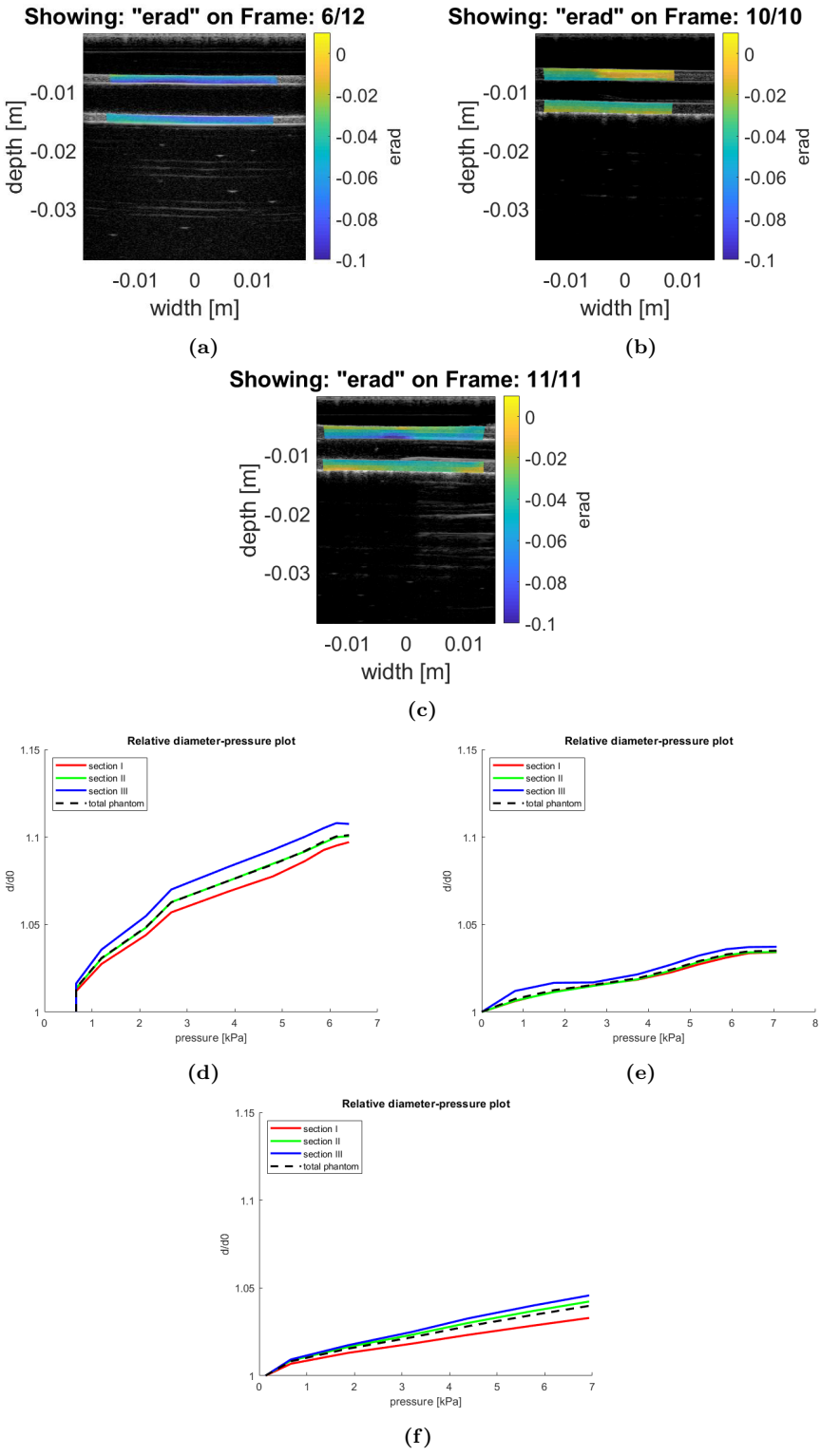

Figure 3.6: **(a)** Radial strain of the normal phantom, **(b)** radial strain of the two tube phantom and **(c)** radial strain of the three tube phantom. While **(b)** and **(c)** show maximum distention, the normal phantom in **(a)** is halfway to maximum distention, but already shows higher radial strains than the tube phantoms. **(d-f)** Relative diameter versus applied pressure plots for each of the three phantoms. **(d)** Normal phantom, **(e)** two tube phantom and **(f)** three tube phantom. The change in diameter for the tube phantoms is considerably lower than that of the normal phantom.

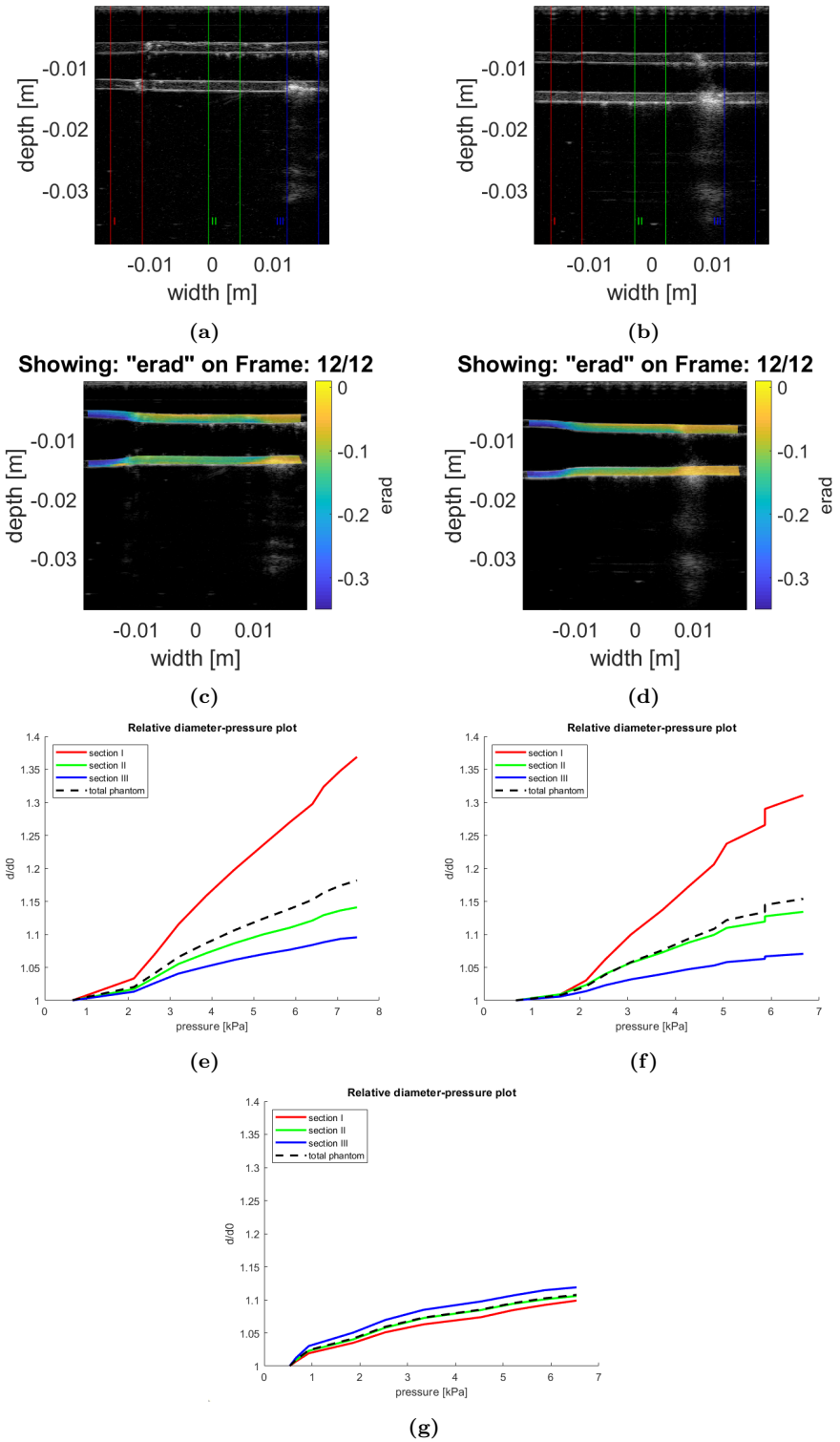

Figure 3.7: **(a-b)** B-mode images are divided into three sections, for both gradient (1) **(a)** as gradient (2) **(b)**. Each section now corresponds to a different number of f/t cycles. Section III of gradient (1) has its left boundary in the border between the middle- and right segment. **(c-d)** The radial strains at maximal distention for gradient (1) **(c)** and gradient (2) **(d)**. It can be seen that for each segment with increased stiffness the overall strain in that segment decreases. **(e-g)** The change in relative diameter in response to the applied pressure for gradient (1) **(e)**, gradient (2) **(f)** and the normal phantom **(g)**. The change in relative diameter decreases for each increase of stiffness with each section. The change in relative diameter of section II of both gradient phantoms resemble the values observed for the normal phantom.

4. Discussion and conclusion

4.1 Discussion

As stated in the beginning of this study, cardiovascular diseases are the leading cause of death worldwide, with stroke being the most prevalent of these diseases. It is currently not yet possible to differentiate between patients with an unstable- and stable plaque, and selection occurs based on the severity of occlusion. Therefore, an improved diagnostic method is necessary to enable the detection of vulnerable plaques. The main objective of this study was in vitro mechanical characterization of vascular phantoms and validation of the elastography method as the first step in mechanical characterization of the carotid (atherosclerotic) wall. For the acquisition of the mechanical properties vascular elastography was utilised and compared with bi-axial tensile testing.

The results show good agreement between the estimated shear modulus from the inflation experiment and the tensile test ($G_{US} = 42 \pm 5$ kPa, $G_{TT} = 37 \pm 6$ kPa). These results are in line with a similar study where also the shear modulus of PVA samples and phantoms was measured, resulting in the following values for the similar phantoms; $G_{US} = 40 \pm 2$ and $G_{TT} = 36 \pm 4$ kPa [Ruijter, 2016]. A study performed by Lopata et al. performed the inflation test and bi-axial tensile test on porcine aortas. The values they found for this vascular tissue were $G_{US} = 112 \pm 11$ kPa and $G_{TT} = 105 \pm 7$ kPa [Lopata et al., 2014]. The model was capable to show lower radial strains around the area of stenosis, as is expected. This did not always correspond with a change in the value of the shear modulus however. This can probably explained with the increase in area size around the stenosis because of thicker walls, also lowering the stress in that area. Further research is needed in order to determine if the elastography method is capable of appointing the correct value of the shear modulus for the stenosis. The vascular elastography model performed very well on the gradient phantoms. For each increase in the number of f/t cycles, an increase in the value of the shear modulus was observed, and the maximal radial strain decreases (figure 3.7). The range of values is in line with the results from the tensile test, showing that the vascular elastography method is capable of accurately perceiving relative changes in stiffness within the phantom.

In order to increase the complexity of the phantoms, attempts of calcification were made. These attempts were not always successful, as well as the first attempt to create these phantoms; the difference between the uncalcified stenosis phantom and the $CaCO_3$ phantom is insignificant, both in shear modulus as maximal radial strain. A possible explanation can be that the particles were too small to have significant impact on the stiffness of the phantom, or that there were not enough particles. The calcification by addition of SiC did also not alter the stiffness of the phantom in any significant way. Some of the attempts with PLA and the addition of tubes filled with a stiffer material promise better results. Changes in relative diameter and maximal radial strain are observed for these phantoms , see figure 3.5 and figure 3.6. The shear modulus for the three phantoms is increased compared to the uncalcified stenosis phantom; 85 kPa, 65 kPa and 65 kPa for the two tube-, three tube- and PLA phantom respectively, versus the $\approx$ 41 kPa of the uncalcified stenosis phantom. As can be seen in figure 3.6 **(b)**, the addition of the tube led to a very local increase in stiffness in the area of the tube, making it a promising method to locally stiffen areas of phantoms. One disadvantage of the current method employed, is that the tube is continuous with one end of the phantom. It would be even better to be able to get the tube in the phantom only in the area around a stenosis, for example.

A general observation regarding the results is that the shear modulus of section III is frequently higher than section I for phantoms where these sections should be identical qua geometry and composition. Section III corresponds to the lateral side of the stenosis, i.e. the side the water (/fluid) will flow last through, before eventually re-entering the phantom at section I. Because pressure is measured at the beginning of the phantom and assumed to be equal for the whole phantom, this can give the false notion that section III has a higher shear modulus than their section I counterpart, as the pressure will fall of gradually along the length of the phantom, especially after a stenosis. An improvement to the setup would then be to also measure the

pressure at the end of the phantom, therefore quantifying the pressure drop over the phantom.

The current model used is the neo-Hookean model which still has its limitations. It assumed a linear elastic, isotropic behaviour and incompressibility of the tissue. The tensile data has revealed that PVA does not behave as a linear elastic material, but as a non-linear, visco-elastic material. This is shown in figure 3.1 **(b)**.

The last paragraphs also pose the question of applicability in the clinic and to in vivo measurements. It has already been shown that pressure can influence the estimation of the shear modulus in this study. In the clinic however, accurate measurement of blood pressure by means of a catheter is invasive, and for an artery like the carotid not an option. The best measurement that could be obtained is probably the brachial pressure. Besides the increased difficulty of pressure estimation in the carotid artery, and the pressure fall around the stenosis, the radial strains will also alter in vivo. In the current inflation experiment there is optimal contrast between the vessel and the surrounding water of the organ bath. In vivo however, there will be surrounding tissue limiting the movement of the vessel and decreasing the contrast of the ultrasound images. Regarding the neo-Hookean model, while PVA did not show linear-elastic behaviour, vascular tissue will not show isotropic behaviour and incompressibility as well [Boekhoven, 2015]. Hyperelastic models have been proposed, which can take into account non-linear elastic behaviour and anisotropy both [van den Broek et al., 2011]. While the accuracy of the arterial wall behaviour would improve, the number of parameters would also increase however. With the clinical setting in mind, this is probably not very feasible, as this means more measurements on thus a higher burden on the patient. Further research is needed to find out which model proposes the ideal balance between patient burden and model accuracy.

Other interesting fields future research could dive into are the creation of more complicated / realistic phantoms. Boekhoven [Boekhoven, 2015] already created phantoms consisting of a fatty plaque around the stenosis, and was able to create double layered phantoms. A next step in this research would be the creation of a double layer phantom with a local calcification (i.e. increased stiffness) around the stenose area. The current phantoms could also be tested for a pressure range more resembling the physiological conditions. While the current study did have a pressure difference of around 40 mmHg, the diastolic pressure was around 0 mmHg. In vivo the same pressure difference can be observed, but the diastolic pressure would then be around 80 mmHg to a systolic pressure of 120 mmHg. Also the application of the elastography method to other areas could be explored. One application that comes to mind is applying this method for patients with aneurysms. Instead of determining the occlusion of the stenose, the diameter of the aneurysm can be imaged. Also in aneurysms the mechanical properties of the wall are important factors in determining if a patient is at risk.

Studies as these are the first steps towards developing a more sophisticated and accurate measurement to asses plaque vulnerability and - stability, hereby preventing stroke and improving the early detection of patients in need for the endarterecomy procedure. The combination of ultrasound imaging and biomechanical modelling could help out future patients a great amount.

4.2 Conclusion

Carotid phantoms were created and vascular elastography was validated by comparing controlled inflation experiments with bi-axial tensile testing. A neo-Hookean model was used to estimate global material properties such as the shear modulus, and the model was able to accurately perceive relative changes in stiffness within the phantom by the use of phantoms with a gradient in stiffness. Future research is needed to determine if the model is capable of appointing the correct mechanical properties for areas of stenosis. The combination of ultrasound and biomechanical modelling has the potential of becoming an important clinical tool in vascular surgery.

Bibliography

[Baldewsing et al., 2006] Baldewsing, R. A., Mastik, F., Schaar, J. A., Serruys, P. W., and van der Steen, A. F. (2006). Youngs modulus reconstruction of vulnerable atherosclerotic plaque components using deformable curves. *Ultrasound in medicine & biology*, 32(2):201–210. 2

[Boekhoven, 2015] Boekhoven, R. W. (2015). Mechanical characterisation of healthy and diseased carotid arteries using ultrasound. 1, 2, 9, 21

[Celermajer et al., 2012] Celermajer, D. S., Chow, C. K., Marijon, E., Anstey, N. M., and Woo, K. S. (2012). Cardiovascular disease in the developing world: prevalences, patterns, and the potential of early disease detection. *Journal of the American College of Cardiology*, 60(14):1207–1216. 1

[Chen et al., 2007] Chen, H., Shi, H., and Varghese, T. (2007). Improvement of elastographic displacement estimation using a two-step cross-correlation method. *Ultrasound in medicine & biology*, 33(1):48–56. 9

[Curtze et al., 2016] Curtze, S. C., Kratz, M., Steinert, M., and Vogt, S. (2016). Step down vascular calcification analysis using state-of-the-art nanoanalysis techniques. *Scientific reports*, 6:23285. 5

[Dabrowski et al., 1997] Dabrowski, W., Dunmore-Buyze, J., Rankin, R., Holdsworth, D., and Fenster, A. (1997). A real vessel phantom for imaging experimentation. *Medical physics*, 24(5):687–693. 3

[Doyley et al., 2000] Doyley, M., Meaney, P., and Bamber, J. (2000). Evaluation of an iterative reconstruction method for quantitative elastography. *Physics in Medicine & Biology*, 45(6):1521. 2

[Elkind, 2006] Elkind, M. S. (2006). Inflammation, atherosclerosis, and stroke. *The neurologist*, 12(3):140–148. 1

[Humphrey, 2002] Humphrey, J. (2002). Cardiovascular solid mechanics: Cells, tissues and organs. 35 springer-verlag. *New York*. 4

[Klabunde, 2011] Klabunde, R. (2011). *Cardiovascular physiology concepts*. Lippincott Williams & Wilkins. 8

[Larsson et al., 2015] Larsson, M., Verbrugghe, P., Smoljkić, M., Verhoeven, J., Heyde, B., Famaey, N., Herijgers, P., and Dhooge, J. (2015). Strain assessment in the carotid artery wall using ultrasound speckle tracking: validation in a sheep model. *Physics in Medicine & Biology*, 60(3):1107. 9

[Lopata et al., 2009] Lopata, R. G., Hansen, H. H., Nillesen, M. M., Thijssen, J. M., and De Korte, C. L. (2009). Comparison of one-dimensional and two-dimensional least-squares strain estimators for phased array displacement data. *Ultrasonic imaging*, 31(1):1–16. 9

[Lopata et al., 2014] Lopata, R. G., Peters, M. F., Nijs, J., Oomens, C. W., Rutten, M. C., and van de Vosse, F. N. (2014). Vascular elastography: a validation study. *Ultrasound in medicine & biology*, 40(8):1882–1895. 2, 7, 20

[Malek et al., 1999] Malek, A. M., Alper, S. L., and Izumo, S. (1999). Hemodynamic shear stress and its role in atherosclerosis. *Jama*, 282(21):2035–2042. 1

[Nave et al., 2015] Nave, A. H., Lange, K. S., Leonards, C. O., Siegerink, B., Doehner, W., Landmesser, U., Steinhagen-Thiessen, E., Endres, M., and Ebinger, M. (2015). Lipoprotein (a) as a risk factor for ischemic stroke: a meta-analysis. *Atherosclerosis*, 242(2):496–503. 1

[Picano and Paterni, 2015] Picano, E. and Paterni, M. (2015). Ultrasound tissue characterization of vulnerable atherosclerotic plaque. *International journal of molecular sciences*, 16(5):10121–10133. 2

[Rothwell and Warlow, 1999] Rothwell, P. M. and Warlow, C. P. (1999). Prediction of benefit from carotid endar terectomy in individual patients: a risk-modelling study. *The Lancet*, 353(9170):2105–2110. 2

[Ruijter, 2016] Ruijter, J. d. (2016). Mechanical characterization of vascular tissue using ultrasound. 4, 20

[Teng et al., 2014] Teng, Z., Brown, A. J., Calvert, P. A., Parker, R. A., Obaid, D. R., Huang, Y., Hoole, S. P., West, N. E., Gillard, J. H., and Bennett, M. R. (2014). Coronary plaque structural stress is associated with plaque composition and subtype and higher in acute coronary syndrome: the beacon i (biomechanical evaluation of atheromatous coronary arteries) study. *Circulation: Cardiovascular Imaging*, 7(3):461–470. 2

[van den Broek et al., 2011] van den Broek, C. N., Van der Horst, A., Rutten, M. C., and Van De Vosse, F. N. (2011). A generic constitutive model for the passive porcine coronary artery. *Biomechanics and modeling in mechanobiology*, 10(2):249–258. 8, 21

[Vancraeynest et al., 2011] Vancraeynest, D., Pasquet, A., Roelants, V., Gerber, B. L., and Vanoverschelde, J.-L. J. (2011). Imaging the vulnerable plaque. *Journal of the American College of Cardiology*, 57(20):1961–1979. 2

A. Appendix

A.1 Protocol PVA preparation

Materials

1. Polyvinyl alcohol (PVA) (Mowiol, 28-99, Sigma Aldrich) with Mw 145,000, 99.0-99.8 mol % hyrdolysis.

2. Ultrasound scatterers (Orgasol 2001, Arkema France), which have an average size of 5.8 m.

3. Scale and heating plate with temperature controller

4. Plastic cup with blue lid and glass beaker (a little bigger than the plastic cup).

5. Magnetic stir bean.

6. Spatula to stir.

7. Soft plastic stopper or small lid (to place on the bottom of the glass beaker, so the plastic cup doesnt get in contact with the glass).

8. Glass stopper (or something else that is a little heavy but small, that you can place on top of the lid of the plastic cup when its in the water so the cup stays put).

Preparation

A solution of 15 wt% (1.25 wt% scatterers))

1. Place the scale and the heating plate with temperature controller in the fumehood.

2. Place the soft plastic stopper in the glass beaker. Fill it with water, be sure it doesnt spill when you place the plastic cup in the water so the top of the lid is at the same height as the edges of the beaker (test this!).

3. Put the glass beaker with water on the plate. Hang the thermometer in the water. Set the temperature of the heating plate at 85C. Set it at high heating speed.

4. Put the stir bean in the plastic cup and place the plastic cup and the lid next to it on the scale (write down the weight). Set the scale to zero.

5. First weigh 1.25 g of scatterers (only take out the plastic bag that contains the scatterers in the fume hood!) put them directly in the plastic cup.

6. Add PVA to a total of 15 g.

7. Carefully add demi H2O to a total of 100 g and stir the mixture with the spatula. Close the lid tightly.

8. When the water is at 85C, carefully place the plastic cup with the PVA solution in the water. Place the glass stopper on top. Turn on the magnetic stir function of the heating plate.

9. Check the solution every 15 minutes and stir with the spatula until the solution becomes om homogeneous.

10. Use the PVA gel directly (for best results) or store at 4C. It stays useable for about 2 weeks. Before using, bring it to room temperature or heat it back up so it becomes less viscous.